THE ASTROPHYSICAL JOURNAL, 496:253–266, 1998 March 20

THE GAUSSIAN PLASMA LENS IN ASTROPHYSICS: REFRACTION

ANDREW W. CLEGG[1]
Naval Research Laboratory, Code 7213, Washington, DC 20375-5351; clegg@intrepid.nrl.navy.mil
ALAN L. FEY
United States Naval Observatory, Code EO, 3450 Massachusetts Avenue NW, Washington, DC 20392-5420; afey@alf.usno.navy.mil
AND
T. JOSEPH W. LAZIO[2]
Naval Research Laboratory, Code 7210, Washington, DC 20375-5351; lazio@rsd.nrl.navy.mil
Received 1996 May 20; accepted 1997 October 30

ABSTRACT

We present the geometrical optics for refraction of a distant background radio source by an interstellar plasma lens, with specific application to a lens with a Gaussian profile of free-electron column density. The refractive properties of the lens are specified completely by a dimensionless parameter α, which is a function of the wavelength of observation, the free-electron column density through the lens, the lens-observer distance, and the diameter of the lens transverse to the line of sight. A lens passing between the observer and a background source, due to the relative motions of the observer, lens, and source, produces modulations in the light curve of the background source. Because plasma lenses are diverging, the light curve displays a minimum in the background source's flux density, formed when the lens is on-axis, surrounded by enhancements above the nominal (unlensed) flux density. The exact form of the light curve depends only upon the parameter α and the relative angular sizes of the source and lens as seen by the observer. Other effects due to lensing include the following: (1) the formation of caustic surfaces, upon which the apparent brightness of the background source becomes very large; (2) the possible creation of multiple images of the background source; and (3) angular position wander of the background source. If caustics are formed, the separation of the outer caustics can be used to constrain α, while the separation of the inner caustics can constrain the size of the lens. We apply our analysis to two sources, which have undergone extreme scattering events: (1) 0954+658, a source for which we can identify multiple caustics in its light curve, and (2) 1741−038, for which polarization observations were obtained during and after the scattering event. We find general agreement between modeled and observed light curves at 2.25 GHz, but poor agreement at 8.1 GHz. The discrepancies between the modeled and observed light curves may result from some combination of substructure within the lens, an anisotropic lens shape, a lens which only grazes the source rather than passing completely over it, or unresolved substructure within the extragalactic sources. Our analysis also allows us to place constraints on the physical characteristics of the lens. The inferred properties of the lens responsible for the scattering event toward 0954+658 (1741−038) are that it was 0.38 AU (0.065 AU) in diameter with a peak column density of 0.24 pc cm^{-3} (10^{-4} pc cm^{-3}), an electron density within the lens of 10^5 cm^{-3} (300 cm^{-3}), and a mass of $6.5 \times 10^{-14}\ M_\odot$ ($10^{-18}\ M_\odot$). The angular position wander caused by the lens was 250 mas (0.4 mas) at 2.25 GHz. In the case of 1741−038, we can place an upper limit of only 100 mG on the magnetic field within the lens.

Subject headings: ISM: general — plasmas — radiative transfer

1. INTRODUCTION

Strong refraction by interstellar electron density irregularities has been invoked to explain several radio astronomical phenomena. Fiedler et al. (1987, 1994a) and Clegg, Fey, & Fiedler (1996) reported a number of extreme scattering events (ESEs)—dramatic changes in the 2.25 GHz flux density—in the light curves of several extragalactic radio sources observed during the course of a 2.25 and 8.1 GHz monitoring program. The changes typically lasted several weeks or months and were occasionally accompanied by strong variations at 8.1 GHz. Because of the simultaneity of the events at different wavelengths, the timescales of the events, and speed-of-light travel time arguments, Fiedler et al. (1987) and Romani, Blandford, & Cordes (1987) concluded that the flux-density variations were likely due to strong scattering by the Galactic interstellar medium (ISM). A similar dramatic change in the flux density and times of arrival has since been observed during a timing program of the pulsar PSR B1937+21 (Cognard et al. 1993).

Interstellar refraction may also be responsible for episodes of multiple imaging and fringing observed in various pulsars' dynamic spectra (Hewish, Wolszczan, & Graham 1985; Wolszczan & Cordes 1987; Gupta, Rickett, & Lyne 1988; Clegg, Fiedler, & Cordes 1993). Dynamic spectra record the flux density of the pulsar as a function of time and frequency. Because a pulsar is an angularly compact coherent emitter, strong interstellar refraction may produce multiple images of the pulsar. The multiple pulsar images

[1] Current address: Millimeter Wave Report, P.O. Box 4749, Arlington, VA 22204-0749; mmwr@msn.com.
[2] NRC-NRL Research Associate.

can then interfere with one another, producing fringes in the time and frequency domains which are visible in the dynamic spectra as alternating bright and dark bands modulating the diffractive scintillation pattern of the pulsar.

The characteristics of the medium responsible for strong interstellar refraction are not clear. For example, it is unknown whether the refraction responsible for such phenomena as ESEs and fringing in pulsar dynamic spectra is the result of a localized large-amplitude electron density enhancement (a "plasma lens") located somewhere between the observer and source, or whether the refraction is the result of an extended turbulent medium with a large number of electron density fluctuations distributed along the line of sight. There are arguments that favor both models: Clegg, Chernoff, & Cordes (1988) showed that expanding shock fronts can naturally create discrete plasma lenses, while the general ISM is widely believed to have an extended, turbulent distribution of electron density fluctuations (Rickett 1990).

To date, refraction phenomena that have been interpreted in terms of the discrete lens model have been analyzed using back-of-the-envelope calculations for the effects of the lens (e.g., Clegg et al. 1993). These calculations have been useful for deriving approximate characteristics of the background radio source and the lens itself. The purpose of this paper is to venture beyond the back-of-the-envelope calculations and to present a detailed, quantitative description of the optics properties of an interstellar plasma lens. The motivation is to present the optics of interstellar plasma lenses in a convenient format that allows application to a wide variety of problems.

In this paper the analysis is limited to the refractive properties of a one-dimensional plasma lens. Results are applied to the specific case of a lens with a Gaussian distribution of free-electron density across the lens plane. The Gaussian lens is a convenient form for describing a plasma irregularity confined to a characteristic size, whose influence on the background wave front is negligible outside of this characteristic size.

The plan of this paper is the following. In § 2 we present a general description of the geometrical optics of a plasma lens, in § 3 we specialize the application to the case of a Gaussian lens form, in § 4 we discuss the light curves expected from a Gaussian plasma lens passing in front of both point and extended sources, in § 5 we discuss the formation of caustics and their utility for extracting information about the lens from the light curve, in § 6 we discuss the expected angular position wander caused by a Gaussian lens, and in § 7 we apply our model to the extreme scattering events seen toward the sources 0954+658 and 1741−038. We summarize our conclusions in the last section.

2. GEOMETRICAL OPTICS OF A PLASMA LENS

The radio-frequency index of refraction n_r in an unmagnetized plasma is

$$n_r^2(\omega) = 1 - \omega_e^2/\omega^2 = 1 - \lambda^2 r_e n_e/\pi \,, \quad (1)$$

where $\omega_e^2 = 4\pi n_e e^2/m_e$ is the square of the electron plasma frequency; e, m_e, $r_e = e^2/(m_e c^2)$, and n_e are, respectively, the electron charge, mass, classical radius, and local number density [$\omega_e = 56\ \mathrm{s}^{-1}\ (n_e)^{1/2}$ for n_e in units of cm^{-3}]; $\omega = 2\pi c/\lambda$ is the angular frequency of the wave; λ is its free-space wavelength; and c is the speed of light.

The phase velocity through the lens is $v_\phi = c/n_r$, which is always greater than c. Compared to the time taken by a wave in vacuum, the phase will traverse a lens of size l in a time $\tau = l(1/c - 1/v_\phi)$ less. In the limit $\omega_e \ll \omega$, which is always true in the case of radio-astronomical observations, the emergent phase from the lens will be advanced by an amount

$$\phi = \omega\tau = \lambda r_e N_e \,, \quad (2)$$

compared to a wave in vacuum, where $N_e = n_e l$ is the column density through the lens. Because the phase is advanced, plasma lenses are *diverging*.

Allow a one-dimensional plasma lens to have a profile of column density $N_e(x)$; implicit in this discussion of a plasma "lens" is the notion that $N_e(x)$ varies across the lens in a regular fashion. A plane wave from an infinitely distant point source is incident on the lens with phase ϕ_0. The phase as a function of x on the emergent side of the screen will be

$$\phi(x) = \phi_0 + \lambda r_e N_e(x) \,. \quad (3)$$

In the geometrical optics limit, rays of energy flux propagate normal to the surfaces of constant phase. As N_e varies across the lens, there will be a slope to the emerging constant phase surfaces. The rays are therefore refracted by the lens through an angle θ_r (Born & Wolf 1980, chap. 3):

$$\theta_r(x) = \frac{\lambda}{2\pi}\frac{d}{dx}\phi(x) = \frac{\lambda^2 r_e}{2\pi}\frac{d}{dx}N_e(x) \,. \quad (4)$$

The observer is a distance D from the lens (Fig. 1*a*). The coordinate in the observer's plane is given by x'. A ray emerging from the plasma lens at coordinate x is refracted by an angle $\theta_r(x)$ and strikes the observer's axis at a position

$$x' = x - \theta_r(x)D \,, \quad (5)$$

for $\theta_r(x) \ll 1$, which will be the case throughout this paper. Multiple solutions $x = x_k$ (with $k = 1, 2, \ldots, n$) to equation (5) can exist for a given x'. In such cases an observer at x' sees n images of the background source appearing to come from the directions toward $x_1, x_2, \ldots, x_n$. The brightness of each image will be enhanced (or reduced) by some factor G_k due to refractive focusing (or defocusing). The factor G_k is determined by the spreading or focusing of rays due to the gradient in refraction angle across the lens:

$$G_k = \left.\frac{dx}{dx'}\right|_{x=x_k} = \left[1 - D\left.\frac{d\theta_r}{dx}\right|_{x=x_k}\right]^{-1} \,, \quad (6)$$

where x_k, as a solution to equation (5), is ultimately dependent on x', D, λ, and the function $N_e(x)$, so that $G_k = G_k[x', D, \lambda, N_e(x)]$.

The same analysis can be modified slightly to account for an angularly extended background source. In this case a

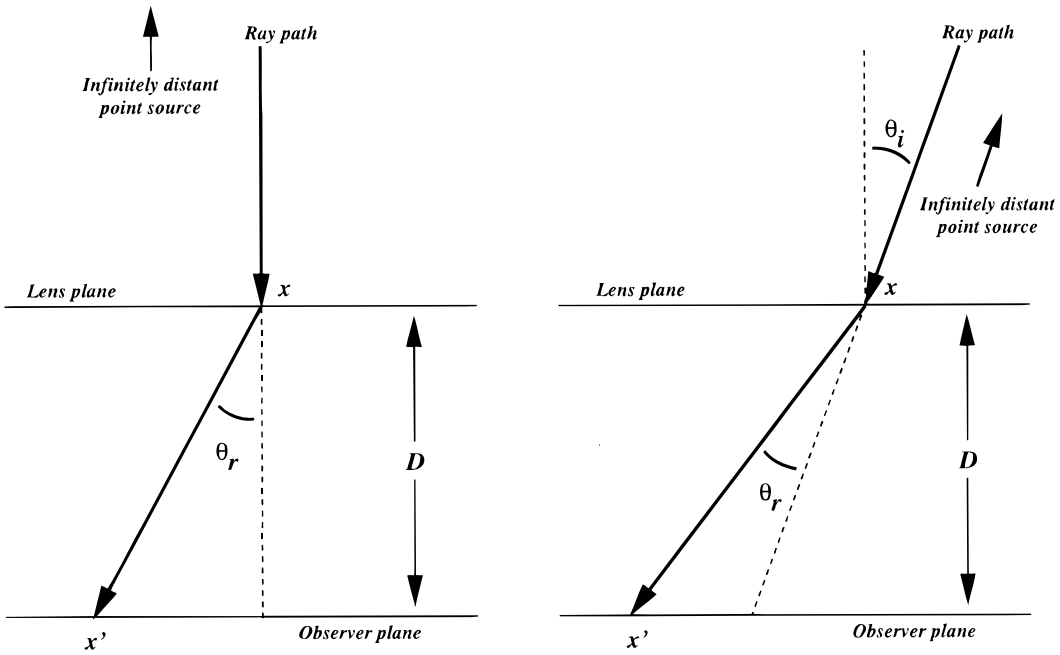

FIG. 1.—Example of ray path geometry through a plasma lens. (*a*) The ray from an infinitely distant point source is incident normal to the lens plane, and strikes the lens plane at the coordinate x. Because of the nonuniform free-electron column density $N_e(x)$, the lens refracts the ray through the angle θ_r. The ray travels the distance D between the lens plane and the observer's plane, and strikes the observer's axis at the point x'. (*b*) The same situation occurs, except that the ray is incident with an oblique angle θ_i upon the lens plane, i.e., the infinitely distant background point source is off-axis.

source of angular extent θ_s is considered to be the superposition of point sources distributed over a range of angles $-\theta_s/2 \leq \theta \leq +\theta_s/2$. For an infinitely distant source, the distribution of rays incident upon the lens screen has a range of incidence angles $-\theta_s/2 \leq \theta_i \leq +\theta_s/2$. The intensity of the rays coming from each incidence angle θ_i is weighted by the function $B(\theta_i)$ to account for the brightness distribution across the source.

For rays incident upon the lens screen with incidence angle θ_i, we obtain

$$x' = x - [\theta_r(x) + \theta_i]D \; . \tag{7}$$

The term $\theta_i D$ in equation (7) accounts for the skewness of the incident ray with respect to the lens axis (Fig. 1*b*). The gain factor G_k is now also dependent on θ_i: $G_k = G_k[x', D, \theta_i, \lambda, N_e(x)]$.

The total observed intensity of the background source is obtained by integrating the product of the gain factor G_k and the source brightness distribution $B(\theta)$ over all θ, and summing the result of this integration over the n images of the background source:

$$I[x', D, \lambda, N_e(x)] = \sum_{k=1}^{n} \int_{-\infty}^{+\infty} B(\theta) G_k[x', D, \lambda, \theta, N_e(x)] d\theta \; . \tag{8}$$

3. THE GAUSSIAN PLASMA LENS

The basis of our analysis of lensing is studying the behavior of $I[x', D, \lambda, N_e(x)]$ in the case where $N_e(x)$ follows a Gaussian distribution in x. The Gaussian distribution is a convenient function for describing a lens that is localized to some region of characteristic size a, and whose refractive strength declines quickly outside of this region. In this section we develop the refractive properties of the Gaussian lens in the limit of geometrical optics. We will show that these properties can be parameterized in terms of a single dimensionless quantity that is constructed from the physical parameters λ, a, D, and $N_e(x)$.

The column density profile takes the form

$$N_e(x) = N_0 \exp\left[-(x/a)^2\right] \; . \tag{9}$$

Following the discussion in § 2, the phase advance due to such a lens is

$$\phi(x) = \lambda r_e N_0 \exp\left[-(x/a)^2\right] \; . \tag{10}$$

The refraction angle, equation (4), becomes

$$\theta_r(x) = -(\lambda^2 r_e N_0/\pi a^2) x \exp\left[-(x/a)^2\right] \; , \tag{11}$$

and the ray path, equation (7), is

$$x' = x\{1 + (\lambda^2 r_e N_0 D/\pi a^2) \exp\left[-(x/a)^2\right]\} - \theta_i D \; . \tag{12}$$

Considerable simplification takes place if the following dimensionless variables are defined:

$$u \equiv x/a \; , \tag{13a}$$

$$u' \equiv x'/a \; , \tag{13b}$$

$$\theta_\ell \equiv a/D \; , \tag{13c}$$

$$\beta_s \equiv \theta_i/\theta_\ell \; , \tag{13d}$$

$$\gamma = u' + \beta_s \; . \tag{13e}$$

The angle θ_ℓ is roughly the angular width of the lens as seen by the observer, while β_s is the incidence angle of the background rays upon the lens screen in units of θ_ℓ.

In the above equations the physical parameters λ, a, D, and N_0 occur consistently in the combination α,

$$\alpha \equiv \frac{\lambda^2 r_e N_0 D}{\pi a^2} = \left(\frac{\sqrt{\lambda D}}{a}\right)^2 \frac{1}{\pi} \lambda r_e N_0 \,. \tag{14}$$

We have written α in this second form to emphasize the essential physics. The phase advance through the lens is $\lambda r_e N_0/\pi$. The Fresnel scale is $(\lambda D)^{1/2}$. Thus, the properties of the lens are determined by the square of the ratio of the Fresnel scale to the lens size and the phase advance through the lens. The larger the parameter α, the greater are the observable effects due to the lens. Hence a weak lens, $\lambda r_e N_0/\pi \ll 1$, can produce large observable effects if the Fresnel scale is sufficiently larger than the lens size. Similarly, a strong lens, $\lambda r_e N_0/\pi \ll 1$, need not produce large observable effects if the Fresnel scale is small relative to the lens size. Numerically,

$$\alpha = 3.6\left(\frac{\lambda}{1\text{ cm}}\right)^2\left(\frac{N_0}{1\text{ cm}^{-3}\text{ pc}}\right)\left(\frac{D}{1\text{ kpc}}\right)\left(\frac{a}{1\text{ AU}}\right)^{-2} . \tag{15}$$

Upon substitution of the above dimensionless variables, the following expressions are derived for the refractive properties of a Gaussian lens:

$$\theta_r(u)/\theta_\ell = -\alpha u \exp(-u^2) \; ; \quad \text{(refraction angle)} \tag{16}$$

$$u[1 + \alpha \exp(-u^2)] - \gamma = 0 \; ; \quad \text{(ray path)} \tag{17}$$

$$G_k = [1 + (1 - 2u_k^2)\alpha \exp(-u_k^2)]^{-1} \; ; \quad \text{(gain factor)} \tag{18}$$

$$I(u', \alpha) = \sum_{k=1}^{n} \int_{-\infty}^{+\infty} B(\beta_s) G_k(u', \alpha, \beta_s) d\beta_s \,. \quad \text{(total intensity)} \tag{19}$$

4. CHARACTERISTIC LIGHT CURVE PRODUCED BY A GAUSSIAN LENS

When transverse motion between source, lens, and observer is assumed, e.g., motion of the observer along the u' axis, $I(u', \alpha)$ translates into a light curve $I(u', \alpha; t, v)$, since $u'(t) = u'(t = 0) + vt$, where t is time and v is the relative transverse velocity. We will show that interpretation of radio light curves in terms of plasma lenses that can be approximated as Gaussian in profile can lead to inferences regarding the physical properties of the lens.

4.1. *General Description*

We will present numerical results in the following sections. Here we will first develop a physical understanding for the basic characteristics of refraction by a Gaussian plasma lens (Fig. 2). Plane waves from an infinitely distant source are incident on the lens screen. The plane waves are indicated by straight dotted lines in the figure, and the lens is represented by a plot showing the electron column density as a function of coordinate u along the lens plane. This representation is purely schematic, as the lens is assumed to have a negligible but uniform width along the line of sight. Upon emergence, the constant-phase surfaces are distorted into contours that mimic the function $N_e(u)$, as represented by the inverse Gaussian–shaped dotted lines. The lines are inverse Gaussian–shaped because the phase velocity is greatest through the center of the lens, where N_e reaches its maximum value of N_0.

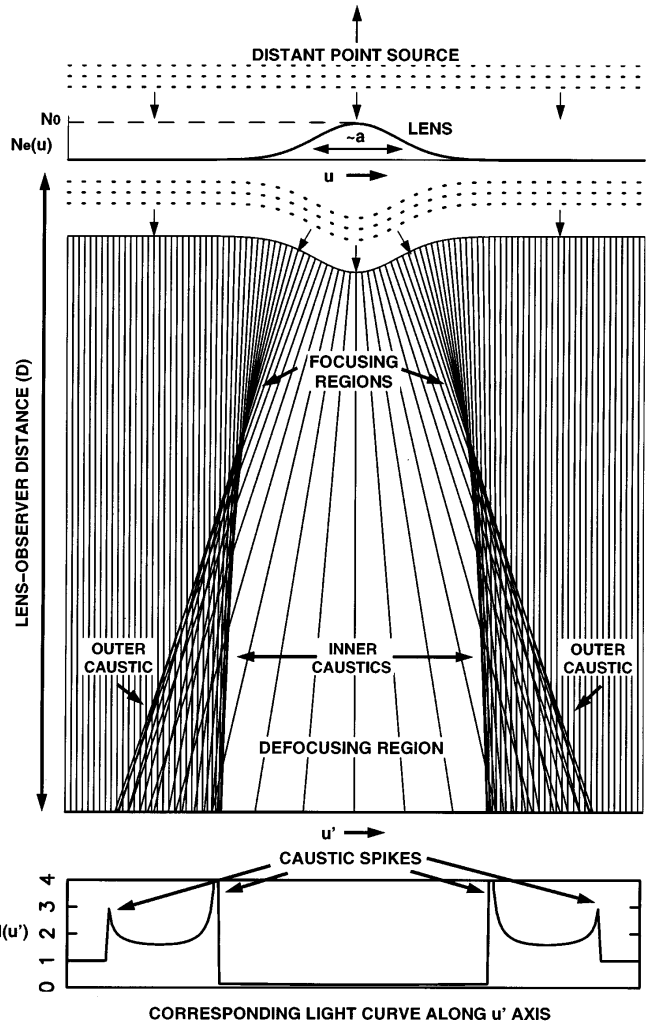

FIG. 2.—Schematic diagram of refraction by a Gaussian plasma lens. See § 4.1 for a complete description of this figure.

In the limit of geometrical optics, the rays of energy flux travel perpendicular to the constant-phase surfaces. The direction of travel of the rays is indicated schematically by the small arrows in the figure. Extending this concept, we have drawn the path of approximately 100 rays as they travel perpendicular to the constant-phase surface after emergence from the lens. The ray path is shown for a total distance D along the lens axis. An observer located close to the lens plane but far from the lens axis (e.g., the upper left and upper right regions of the ray trace) sees an unchanged source: There is no change in the observed flux density (no change in the number density of the rays) or in the source's position (the direction of arrival of the rays).

Somewhat farther from the lens and slightly off-axis, in the "Focusing Regions" marked in Figure 2, the rays begin to converge and their number density increases. An observer located in this area of the ray trace would see a source of enhanced brightness somewhat displaced from its "true" position, as evident from the increased number density and skewness of the rays, respectively. At the same distance from the lens, but closer to the lens axis, the rays are spread apart by the lens. An observer in this region would see a source of decreased brightness due to the lower number density of rays. The source would be offset from its true position by an

amount that increases with the observer's distance from the lens axis. Directly on the lens axis, the number density of rays reaches a minimum, but the source appears in its correct position.

At a larger distance from the lens plane, the skewed rays that make up the focusing regions cross one another. Inside this region where the rays have crossed, more than one bundle of rays would be incident on an observer. Each bundle would appear to come from a different direction. The observer therefore sees more than one image of the background source. In the case of a Gaussian lens, the greatest number of images seen is three. Since each ray bundle arrives from a different part of the lens, the spreading of the rays in each bundle, and therefore the brightness of the particular image represented by each bundle, may differ.

Outside the focusing region, only a single image is seen. At large distances from the lens axis, the image has its nominal brightness, as evident from the uniform density and straight path of the rays in this region. Close to the lens axis the image has a reduced brightness as evident from the spreading of rays in this region.

Separating the single image regions from the multiple-image regions are the caustic surfaces. On these surfaces, an observer sees multiple images merge into a single image, and the local number density of rays from that image grows without bound in the limit of geometrical optics. In the case of a Gaussian lens, two of the three images merge on the caustic surface. In reality, the brightness of the image is limited by diffraction effects, which are not taken into account here.

Now assume that an observer, due to relative transverse motion of the lens, travels at a constant (large) distance D from the lens plane. The transverse coordinate along the observer's path is given by u', which is a function of time t. As the observer encounters different ray densities, the brightness of the background source (and its apparent position) will change with time. At the bottom of Figure 2 is a light curve constructed by plotting the number density of rays encountered as the observer travels across the bottom of the ray trace. The intensity I is normalized to unity in the absence of the lens. In the multiple-imaging regions, the observed brightness is taken as the sum of the number densities of the ray bundles that reach the observer, in accordance with equation (8).

When the observer crosses a caustic surface, the number density of rays tends toward infinity (for geometrical optics), and therefore the observed brightness of the source becomes very large. In our refraction simulations, this increase in intensity is represented by tall spikes in the light curve. The height of the spikes is generally not properly represented in refraction simulations, but their existence is correct qualitatively.

4.2. *Numerical Results*

4.2.1. *Point Source*

We start by considering the refraction of a background point source by a Gaussian lens. In this case $\beta_s \equiv 0$, and we take I_0 to be the intensity of the background source in the absence of lensing. The observed intensity, equation (19), reduces to

$$I(u', \alpha) = I_0 \sum_{k=1}^{n} G_k(u', \alpha) \, . \tag{20}$$

For a given value of α, the function $I(u', \alpha)$ is determined in practice by numerically computing the root(s) u_k of equation (17) (which is a transcendental function) for a particular u', then computing the gain factor(s) G_k of equation (18) and performing the sum in equation (20). This is done for a range of u' to construct the light curve.

As an initial example, consider a Gaussian plasma lens with peak electron column density $N_0 = 0.1$ pc cm^{-3} and width $a = 2$ AU. The observer is located at a distance $D = 1$ kpc away and is observing at a wavelength $\lambda = 20$ cm. For this particular combination of physical parameters, $\alpha = 36$ (eq. [15]); other combinations can also produce similar values of α. Equations (16)–(19) have been solved over the range $-20 \leq u' \leq 20$ for this value of α, and $\sum G_k$ for each u' is plotted in Figure 3. The plot represents the enhancement (or decrease) in the brightness of the background point source over its value in the absence of a lens. The features in the light curve follow the general discussion in the previous section. On the lens axis, $u' = 0$, there is one image and the intensity is at a minimum, with a gain factor of $G_1 = 0.027$ in accordance with $1/(1 + \alpha)$, as predicted by equation (18).

Other values of α will give different light curves. Larger α gives rise to greater transverse displacement of the rays. This can occur by the following: (1) increasing the distance D between observer and lens; (2) increasing the maximum column density N_0 or decreasing the characteristic size a so that the transverse gradient of the column density, and therefore the refraction angle, becomes greater; or (3) observing at a longer wavelength, where the index of refraction n_r becomes smaller (greater deviation from 1).

Light curves are shown for various values of α in Figure 4. Consider first the cases of weak refraction, $\alpha = 0.1$ and $\alpha = 1$. The transverse displacement of the rays is small and no ray crossing occurs. Modulations in the light curve are due solely to focusing and defocusing of the ray bundles, since there are no caustics. When α is increased to 5, the onset of ray crossing is evident from the existence of caustic spikes. However, the observer is close to the distance D, where ray crossing just begins to occur. This is evident from the close proximity between the inner and outer pairs of caustics, compared to the width of the defocusing region near the lens axis (cf. Fig. 2). We will say more in § 5 on the distances between caustics and what that tells us about the

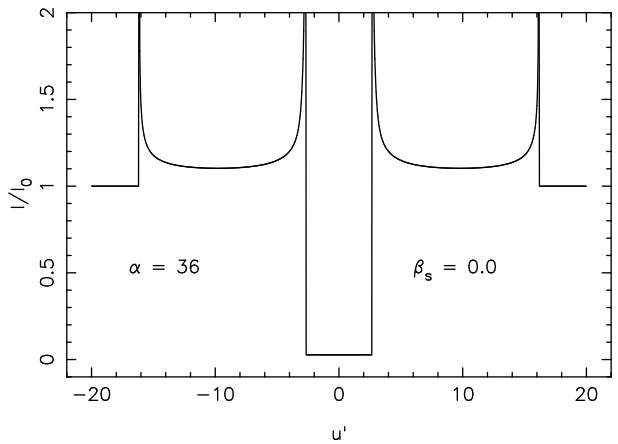

FIG. 3.—Light curve of an infinitely distant point source refracted by a lens with $\alpha = 36$.

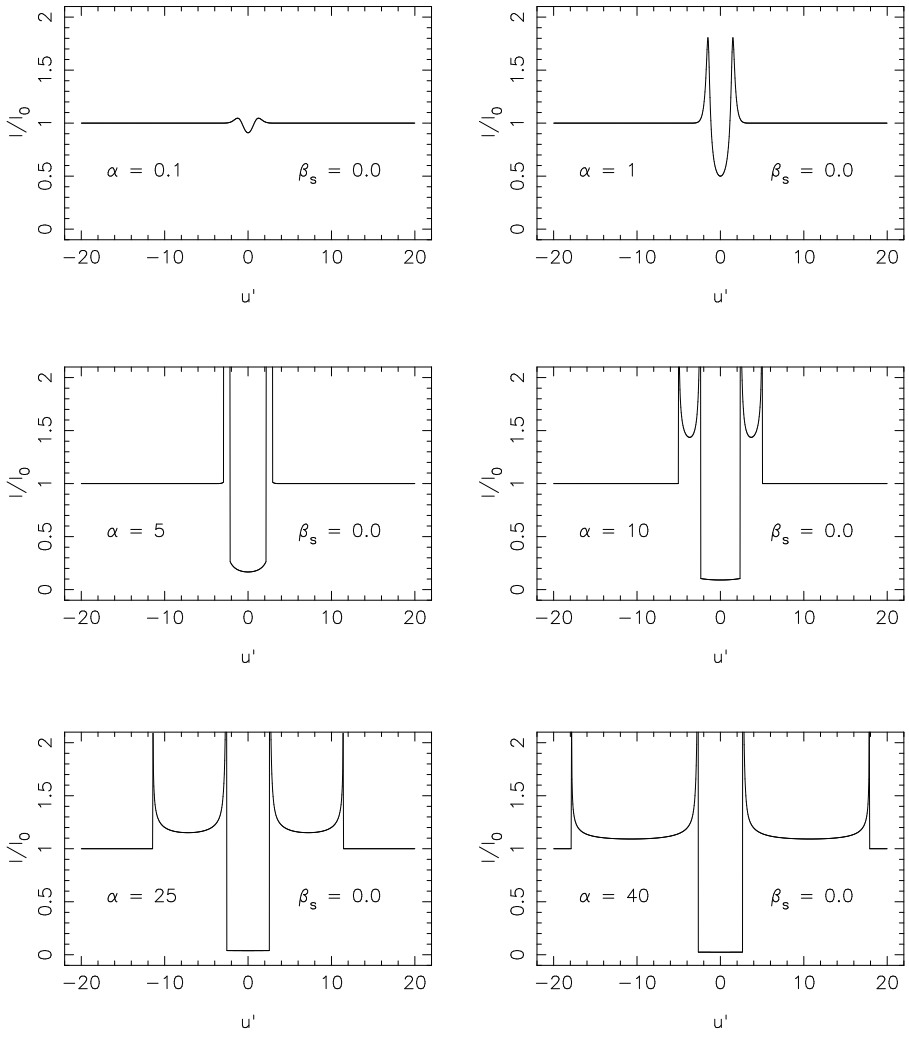

FIG. 4.—Light curves produced by refraction through lenses with a range of values of α, as defined by eq. (15)

lens. Moderate refraction is shown by the example $\alpha = 10$. The pairs of caustics have moved farther apart and the minimum in the light curve on the lens axis becomes deeper: 1/11 of its nominal value. The light curve for $\alpha = 40$ exhibits strong refraction. The outer pair of caustics forms very far from the lens axis, near the limits of the plot, while the inner pair is not as strongly affected. This fact will be exploited in § 5 to estimate the size of the lens based on observed light curves. On-axis, the source is only 1/41 of its nominal brightness.

4.2.2. *Extended Source*

For an extended source the effect of the lens is determined not only by α, but also by the relative angular extent of the source compared to the angular extent ($\sim a/D$) of the lens. Since we will generally invoke a Gaussian brightness distribution across the source, the parameter β_s is taken as the ratio of the FWHM angular width of the source to the observed angular FWHM of the lens.

The numerical simulations are shown in Figure 5. Using an $\alpha = 25$ lens we show the light curve from a point background source, $\beta_s = 0$, as well as those for $\beta_s = 0.1$, 0.25, 0.5, 1.0, and 5.0. It is evident that an extended source smoothes out the caustic spikes and the transition into the defocusing region near the lens axis. However, the brightness minimum at the center of the lens remains substantial until the source is larger than the lens. For instance, when $\beta_s = 1$ the on-axis gain is 0.039, only 2% larger than the gain $1/(1 + \alpha)$ predicted by a point source. When the source is much bigger than the lens, the result of refraction is to produce a ripple rather than strong modulations in the light curve. Rays from the outer edges of the source are refracted into the defocusing region, so the minimum intensity is not as deep as for a point source.

Note that the height of the ripple and the true effects on the caustic spikes of an extended source cannot be quantitatively determined without a simulation that also includes diffraction effects. We have performed limited diffraction simulations and can say that the refractive light curves are correct in a qualitative sense.

5. THE CAUSTICS

The caustics are a powerful probe of the physical properties of the lens. In our refractive simulations the important observable is the distance between the pairs of caustic spikes. Diffractive fringes form in the vicinity of the caustics due to interference between the multiple images. Although it is beyond the scope of this paper, the fringes can serve as a useful probe of both the lens and the background source (e.g., Wolszczan & Cordes 1987).

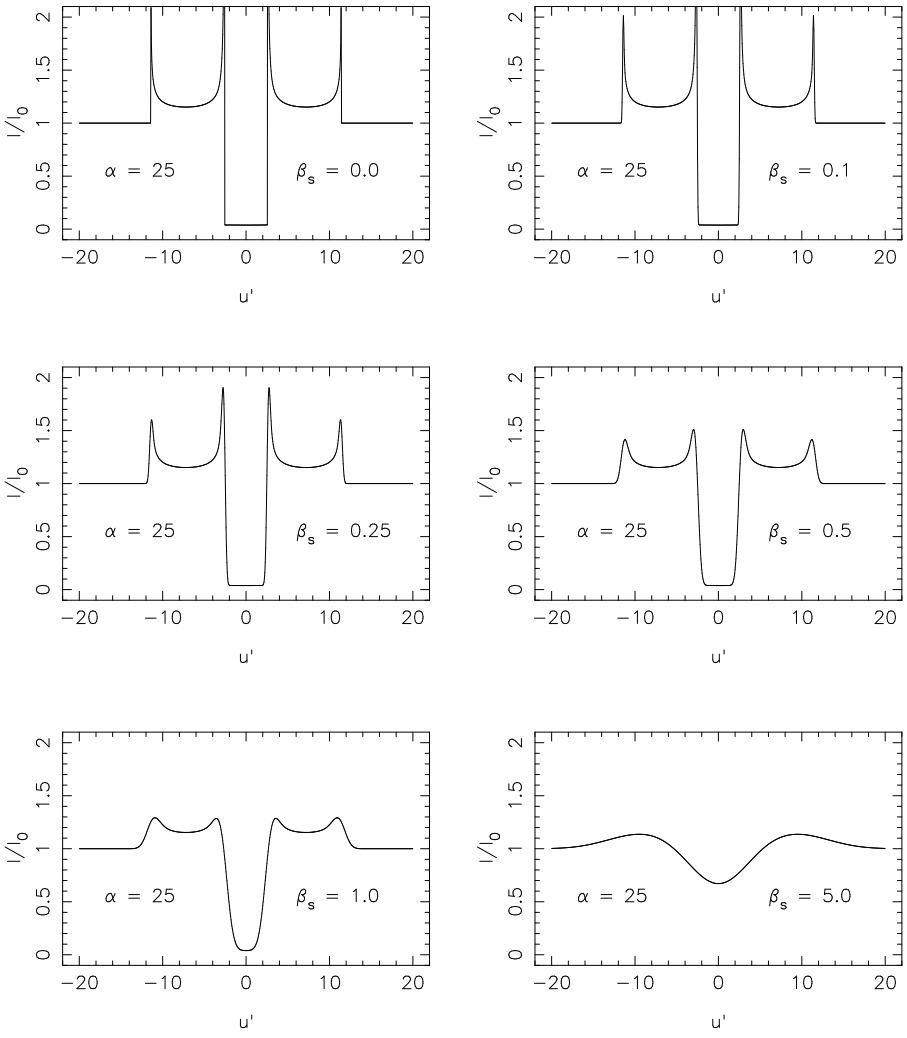

FIG. 5.—Light curves produced by an $\alpha = 25$ lens, with various relative angular sizes of background source and lens. The parameter β_s is the angular size of the (unlensed) background source in units of the angular size of the lens, as seen by the observer.

As evident from Figure 4, the distance between the inner two caustics measured in units of the characteristic size a of the lens is a relatively weak function of α, while the distance between the outer two caustics depends more strongly on α. We have solved for the locations where the caustics intersect the u'-axis, as a function of α. We define the dimensionless quantities $\Delta u_i'$ and $\Delta u_o'$ as the distances between the inner and outer pairs of caustics, respectively, in dimensionless units of u'. These quantities are plotted as functions of α in Figure 6, where we have also plotted $(\Delta u_o' - \Delta u_i')/2$, the distance between the outer and inner caustics on each side of the lens axis. It is evident from the figure that no caustics form if $\log_{10} \alpha < \log_{10} \alpha_{\min} \simeq 0.35$ ($\alpha_{\min} \simeq 2.25$). In this case the observer is closer to the lens than to the point at which ray crossing occurs. For $\alpha = \alpha_{\min}$, caustics have formed but the inner and outer caustics are merged together. As α increases, the outer pairs spread apart, while $\Delta u_i'$ remains relatively fixed.

Although these separations are derived from solutions to transcendental equations, it is possible to find an analytic expression for $\Delta u_o'$ as a function of α, the derivation of which we present in the next section. For $\Delta u_i'$ we have performed a linear least-squares fit in the log-log domain to find an approximate functional dependence on α. The separations are

$$\Delta u_i' \approx 4.30\alpha^{0.055} \; ; \tag{21}$$

$$\Delta u_o' = \sqrt{2}(1 + \alpha e^{-1/2}). \tag{22}$$

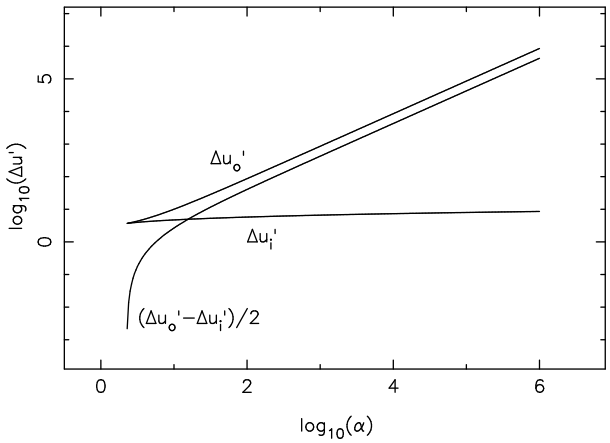

FIG. 6.—Separation between the outer caustics, $\Delta u_o'$; between the inner caustics, $\Delta u_i'$; and between the pairs of caustics on either side of the lens axis, $(\Delta u_o' - \Delta u_i')/2$, as functions of the parameter α.

The dimensionless quantity $\Delta u_i'$ is $\Delta x_i'/a$, where $\Delta x_i'$ is the distance between the inner two caustics. The characteristic size a of the lens can therefore be estimated as $a \simeq \Delta x_i'/4.3$. Additionally, the value of α can be estimated by measuring the relative separations between the inner and outer pair of caustics:

$$\alpha \simeq 1.7\left(3\,\frac{\Delta x_o'}{\Delta x_i'} - 1\right)^{1.06}, \tag{23}$$

where $\Delta x_o'$ is the distance between the outer pair of caustics.

We emphasize that the distance between the inner pair of caustics is the *only reliable estimate for the size of the lens.* Using the value $\Delta x_o'$ determined through observations of the total duration of the lensing event to judge the size of the lens is not appropriate; see Figure 6. It can deviate by a factor of order α from the true characteristic size a of the lens. Since physically plausible values of α can exceed 10^4, a characteristic lens size derived from the total duration of the lensing event will overestimate the true size by a comparable factor.

6. ANGULAR DISPLACEMENT

In addition to changes in the observed brightness of the lensed source, the plasma lens also causes variations in the apparent angular position of the source. Consider an observer at a point u', who observes a ray that, as a solution to equation (17), comes from the point u_k on the lens plane. In the small-angle approximation, the angular displacement of the source from its "true" (unlensed) position is $(u' - u_k)\theta_\ell$; see equation (5). The value of $(u' - u_k)$ depends on u and the parameters α and β_s. For simplicity, we will restrict our discussion to the case of a point source, for which $\beta_s = 0$.

Figure 7 shows the general behavior of the angular displacement of a background source as viewed through a plasma lens. While this figure was computed for one particular value of α, the qualitative form of the angular displacement is independent of α. The figure shows the function $(u' - u_k)$ for valid solutions of equation (17) as a function of u'. The lens axis intersects the observer's axis at $u' = 0$. The vertical axis, both in contour plot form and in a pseudo–three-dimensional form, is the relative intensity of the image coming from a particular value of $(u' - u_k)$. At values of u' far from the lens axis, e.g., $u' = 5$, $(u' - u_k) = 0$, there is no angular displacement (image A in the figure). Closer to the lens axis, the outer caustic is formed, e.g., near $u' = 3.1$. In Figure 7 the caustic is evident by the sudden formation of a second bright image at a new value of $(u' - u_k)$. Image A also remains; i.e., $(u' - u_k)$ as a function of u' becomes multivalued. The new bright image is angularly displaced from the "true" position of the background source as evident from the nonzero value of $(u' - u_k)$.

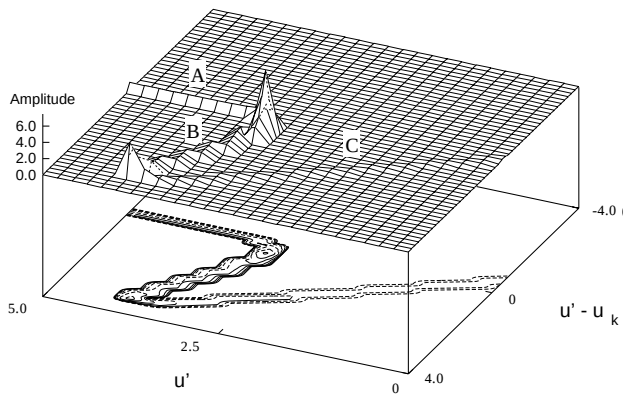

FIG. 7.—Brightness and angular displacement of images formed by the Gaussian plasma lens as functions of observer position u'. See § 6 for a complete description of this figure.

Even closer to the lens axis, the image from the caustic breaks up into two separate images (B and C in the figure), and their intensities diminish. Image B moves toward the original image (image A) as u' decreases, i.e., as one moves closer to the lens axis. The intensity of image C diminishes quickly.

Somewhat closer to the lens axis, the inner caustic forms, e.g., $u' \approx 2.6$, where images A and B merge into a single very bright image. Then, images A and B disappear altogether, leaving only the weak image C. This image moves toward zero angular displacement as the observer nears the lens axis, $u' = 0$. On the axis, image C has zero angular displacement and reaches its minimum flux density, $1/(1 + \alpha)$ of the nominal source intensity.

The magnitude of the angular displacement can be estimated from equation (5). The angular displacement in radians for an image from a point u_k on the lens plane reaching the point u' on the observer plane is

$$\delta\theta = (u' - u_k)\theta_\ell\,, \tag{24}$$

where we have assumed that the lens axis passes through $u = u' = 0$. For a Gaussian lens, the ray-path description, equation (17), gives u' in terms of the solution(s) u_k,

$$(u' - u_k) = u_k\,\alpha\,\exp\,(-u_k^2)\,. \tag{25}$$

The maximum value of the difference $(u' - u_k)$ occurs for $u_k = 1/2^{1/2}$, which is a solution to equation (17) when the observer is located at the point $u' = (\alpha e^{-1/2} + 1)/2^{1/2}$. The total separation between the two outer caustics is twice this value, from which equation (22) is derived. This expression is true for all α.

In Figure 7 it is evident that the maximum angular displacement occurs as the observer crosses the outer caustic. Images B and C are merged into one image there. Since the image is coming from the point $u_k = 1/2^{1/2}$ and the observer is at the point $u' = (\alpha e^{-1/2} + 1)/2^{1/2}$, the angular displacement of the merged image is

$$\delta\theta = (u' - u_k)\left(\frac{a}{D}\right) = \frac{1}{\sqrt{2}}\,\alpha\theta_\ell\,e^{-1/2}\,. \tag{26}$$

7. APPLICATION TO EXTREME SCATTERING EVENTS

We have presented a quantitative analysis of the refractive properties of a specific optical system: a one-dimensional interstellar plasma lens. The specific case of a Gaussian distribution of electron density transverse to the line of sight has been considered. We do not believe that such ideal systems exist in reality, but the results of our analysis provide a starting point for a semiquantitative analysis of extreme scattering events toward distant radio sources.

Fiedler et al. (1994a) summarized the variety of light curves observed during ESEs. The scattering events are pronounced at lower frequencies ($\approx$1 GHz), but usually weakly detected or not detected at higher frequencies ($\sim$10 GHz), presumably due to a combination of weaker ISM scattering

at shorter wavelengths and intrinsic noise in the radio light curves. One exception to this general rule is the first detected scattering event, toward the quasar 0954+658, which occurred in 1981. At 8.1 GHz, the most prominent features in the light curve are four strong spikes, reminiscent of caustic spikes due to a pointlike source being refracted by a strong lens.

The lack of caustic spikes in most of the identified ESEs, however, implies that the typical plasma lenses that produce ESEs are fairly weak (small α), so that multiple imaging does not occur; the lenses have much smaller angular diameters than the background sources (large β_s), so that caustic surfaces are less pronounced; or a combination of both effects. Fey, Clegg, & Fiedler (1996) present multiepoch, multiwavelength images of sources in which an ESE has been identified at times when the sources were not undergoing an ESE. They find the sources to be compact with typical FWHM diameters of approximately 1 mas at wavelengths between 3.5 and 18 cm. Figure 5 indicates that, if the lack of caustic spikes is because the lenses have smaller angular diameters, the typical lens diameter would be $\theta_\ell \lesssim 0.1$ mas (0.1 AU at 1 kpc). We therefore favor the weak-lens model as the most plausible explanation for the general lack of caustic spikes in ESEs.

The best-studied ESE is that for the extragalactic source 1741−038, which occurred in 1992. High-quality light curves were obtained at 2.25 and 8.1 GHz during the event, and refraction effects were detected in both. Radio polarization data obtained during the event and 1.5 yr afterward have been used to constrain the magnetoionic structure of the lensing medium (Clegg et al. 1996). VLBI observations of 1741−038, also obtained outside the ESE, have been used to determine the unlensed angular structure of this source. Fey et al. (1996) used these data in conjunction with the Fiedler et al. (1994a) model to infer that the angular diameter of the lens and the source must be comparable ($\approx$0.5 mas).

We have chosen the ESEs toward 0954+658 and 1741−038 for detailed analysis with respect to our Gaussian lens model. This choice was made due to the apparent formation of caustics during the 0954+658 event and the quality of the data obtained during the 1741−038 event. In the following discussion, we will obtain semiquantitative estimates of lens parameters and indicate how additional data would be useful in improving our estimates.

7.1. *0954+658*

The 2.25 and 8.1 GHz light curves obtained for 0954+658 are shown in Figure 8. The ESE, which occurred in 1981, is shown in Figure 9 on an expanded scale. The 2.25 GHz ESE is marked by a flat-bottomed minimum, at which the flux density of the source is one-half its nominal (unlensed) value, surrounded by two peaks, which we identify below as the inner two caustics. The 8.1 GHz ESE is marked by a 2 Jy peak and three 1 Jy peaks bracketing an approximately 1.5 month minimum in the source's flux density. The minimum is less pronounced at 8.1 GHz, as the source's flux density during the event decreases to 70% or so of its nominal value. Below, we identify these four, approximately 1 Jy peaks as the caustics.

The flat-bottomed minimum in the 2.25 GHz ESE indicates that, at this frequency, the intrinsic angular diameter of 0954+658 is substantially smaller than the angular diameter of the plasma lens; see Figure 5. However, the fact that the flux density during the ESE only decreases to one-half its nominal value can be reconciled with our lens model only if the light curve is the sum of a lensed and an unlensed component. If we take the amplitude of the light curve during the minimum to be the flux density of the unlensed component, the light curve can be represented by a two-component source model in which a component of flux density 0.35 Jy is lensed by the intervening medium and a second component of flux density 0.3 Jy is unaffected by the lens; the angular diameter of the lensed component also has to be sufficiently small enough to produce the flat-bottomed minimum.

The unlensed component could be either a compact component of 0954+658, such as a jet component, whose line of

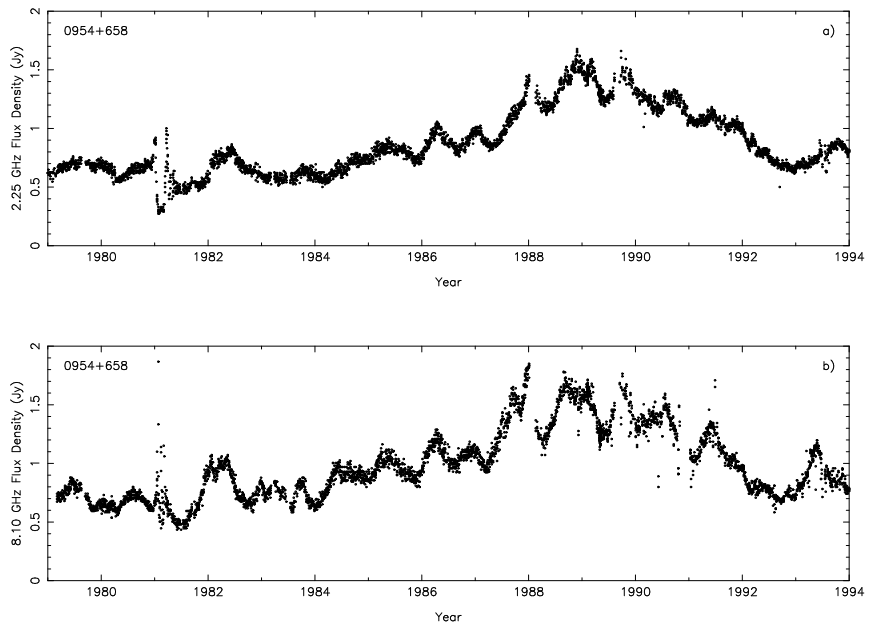

FIG. 8.—Complete light curve of the quasar 0954+658 during the period of observation from 1979 to 1994. The scattering event occurs at approximately 1981 January.

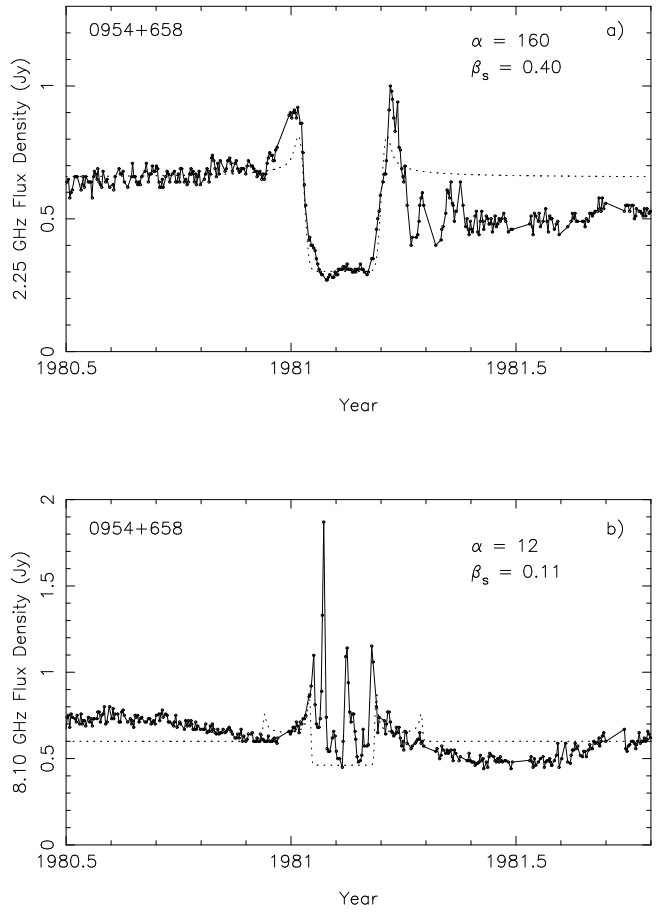

FIG. 9.—Light curve of the quasar 0954+658 during an extreme scattering event. (*a*) Data obtained at 2.25 GHz, compared to our lens model (*dashed line*) with $\alpha = 160$ and $\beta_s = 0.4$. A two-component model for 0954+658 was used: a lensed component of flux density 0.35 Jy, and an unlensed component of flux density 0.3 Jy. (*b*) Comparison of the 8.1 GHz data and a two-component model with $\alpha = 12$, $\beta_s = 0.11$, lensed flux density 0.15 Jy, and unlensed flux density 0.45 Jy.

sight was unaffected by the lens, or emission on larger scales, which is completely resolved by VLBI arrays but is unresolved to the much smaller Green Bank Interferometer used to obtain the light curve. Both scenarios are consistent with the observed structure of 0954+658.

Gabuzda et al. (1992, 1994) conducted 5 GHz observations between 1987 and 1989, and found the source to consist of a compact core (<0.5 mas) with a jet extending approximately 5 mas to the northwest. Within the jet they identified multiple, compact (<1 mas) knots. With the possible exception of the knot K0 (Gabuzda et al. 1994), however, none of the knots they identified would have been present at the time of the ESE. The proper motion of the knots is approximately 0.4 mas yr^{-1}, large enough that most of the knots were not ejected until after the ESE (epoch 1981.1), unless the knots have undergone substantial acceleration since their ejection. Pearson & Readhead (1988) included this source in a finding survey conducted in 1978. Although they did not image it, they found it to be compact and poorly modeled as a single Gaussian component. These VLBI observations bracket the time of the ESE and found indications of compact, yet complex structure. We therefore conclude that it is plausible that, at the time of the ESE, the source consisted of multiple compact components, whose typical angular scales are milliarcseconds.

On intermediate to larger angular scales, tens of milliarcseconds to arcseconds, there is also emission from this source. Gabuzda et al.'s (1992, 1994) VLBI observations also included simultaneous VLA observations. They found that approximately 15% ($\approx$0.15 Jy) of the flux was resolved out by the VLBI observations. Also, using lower resolution VLA observations Kollgaard et al. (1992) find a jet extending approximately 4″ to the south of the VLA core; the jet's flux density is approximately 0.22 Jy. This extended emission would lie entirely within the synthesized beam of the Green Bank Interferometer, but would be unaffected by the passage of a Gaussian lens in front of the source. In summary, this source displays emission on a range of angular scales, from submilliarcseconds to arcseconds. A combination of small-scale components, whose line of sight the lens did not intersect, and emission on larger scales could provide the 0.35 Jy of unlensed flux.

To obtain quantitative estimates of the lens parameters, we proceed as follows. We obtain approximate values for α and β_s by appeal to the light curves. We refine our estimates for α and β_s by producing simulated light curves with slightly different values of α and β_s and comparing visually the simulated and actual light curves. Due to the simple model we are considering here, we judged a more exhaustive search of the (α, β_s) parameter space not to be worthwhile.

Comparing the shape of the inner caustics and minimum of the 2.25 GHz ESE to Figure 5, we estimate β_s to be $0.1 < \beta_s < 1$. From the separation of the inner and outer caustics in the 8.1 GHz ESE and equation (23), we estimate $\alpha \approx 10$ at this frequency. Since $\alpha \propto \lambda^2$, at 2.25 GHz we have $\alpha \approx 130$.

Varying the parameters and comparing simulated light curves to the actual 2.25 GHz light curve, we find reasonable agreement for $\alpha = 160$ and $\beta_s = 0.4$. In Figure 9 we have superposed the simulated light curve for this set of parameters on the 2.25 GHz light curve of 0954+658. In doing so, we have scaled the u' axis arbitrarily since it depends on the unknown relative transverse velocities of the observer and lens. The agreement with the ESE minimum is good. The simulation underestimates the amplitude of the inner pair of caustics. The outer caustics for $\alpha = 160$ are far outside the time range of the observations plotted in Figure 9. We have compared our simulation to the full time range of the observations of 0954+658 (Fig. 8). We do not see any evidence for the existence of the outer caustics, but the predicted amplitude of the outer caustics is significantly smaller than the predicted amplitude for the inner caustics. The outer caustics are probably lost in the noise in the light curve. The ESE occurs during a general decrease in the source's flux density, probably caused by intrinsic variations. This general decrease in the source's flux density explains the lack of agreement between the amplitude of the actual light curve and the model light curve after the ESE.

To compare our model with the 8.1 GHz light curve, we scale the light-curve fit to the 2.25 GHz ESE to 8.1 GHz. We believe such a simple scaling is justified within the context of our one-dimensional simulations of a Gaussian lens passing in front of a single compact component of 0954+658. Below we discuss briefly the consequences of relaxing the assumptions in our simple model.

We assume that the angular size of the lensed component of 0954+658 scales as λ, as is generally appropriate for

flat-spectrum extragalactic radio sources. Although the refractive index within the lens does change with wavelength, the physical size of the lens should not. Thus, the relative angular extent of the lensed component is (2.25/8.1) = 0.28 times smaller at 8.1 GHz as compared to 2.25 GHz or $\beta_s = 0.11$ at 8.1 GHz. Our estimated value of α at 2.25 GHz, $\alpha = 160$, corresponds to $\alpha = 12$ at 8.1 GHz. The resulting model light curve is superposed on the actual light curve in Figure 9. The best match for the flux densities of lensed and constant components at 8.1 GHz is 0.15 and 0.45 Jy, respectively.

We identify tentatively the lensed component of 0954+658 as a jet component, not the core. The difference in flux density at the two frequencies for the lensed component, 0.35 Jy at 2.25 GHz to 0.15 Jy at 8.1 GHz, indicates that the lensed component has a steep spectrum, $S \propto \nu^{-0.7}$. The emission from the source at 5 and 8 GHz is dominated by compact components (Gabuzda et al. 1992, 1994; Gabuzda & Cawthorne 1996; unpublished VLBI observations), generally with flat spectra (viz., Fig. 8). However, one of the two knots in the jet, knot K3 (Gabuzda et al. 1994; Gabuzda & Cawthorne 1996) has a similar spectral index with a 5 GHz flux density of 0.2 Jy. We reiterate that, because of proper motions, none of the knots seen at 5 GHz by Gabuzda et al. (1994) or at 8 GHz by Gabuzda & Cawthorne (1996) would have been present at the time of the ESE. Nevertheless, we believe the existence of such a jet component at a later date suggests that such a component could have been present during the ESE. Clearly VLBI observations during and after an ESE would be quite useful in assessing which component(s) was lensed.

Qualitatively, Figure 9 shows that our simulation reproduces the four caustic spikes in the 8.1 GHz light curve. However, the timescale for the scattering event derived from our model differs substantially from the observed data. The model predicts a duration of approximately 0.4 yr, while the observed duration is about half of that. Equation (22) and Figure 6 show that the distance (and therefore timescale) between the inner pair of caustics is a very weak function of α in our model, and, therefore, a very weak function of observing wavelength. In essence, the timescale between the inner caustics at 2.25 and 8.1 GHz should be nearly identical. In the observational data, that is not the case.

The most likely explanations for the discrepancy between our model and the data are due to the limitations of a one-dimensional lensing simulation. The wavelength scaling of the timescale of the lensing event derived in the one-dimensional model does not account for the possibility that the midpoint of the lens may not cross the background source. Instead, only a chord of the lens, rather than the full diameter, may pass in front of the background source. Combined with complex wavelength-dependent structure in the background source, meaning that the predominant contribution to the flux density may shift in position with wavelength, the net effect will be a complicated wavelength scaling of the timescale for the lensing event.

We use our estimates of α and β_s to constrain the physical properties of the lens. Since the better comparison is obtained at 2.25 GHz, we will use the parameter values found at that frequency: $\alpha = 160$, $\beta_s = 0.4$. From equation (15), the maximum electron column density through the lens is

$$N_0 = 0.28 \text{ pc cm}^{-3}\ \alpha\lambda^{-2} D\theta_s^2 \beta_s^{-2}\ . \qquad (27)$$

Here θ_s is the angular size of the background source in units of milliarcseconds, and we have used the fact that $\beta_s \equiv \theta_s/\theta_\ell$ from equation (13).

The unknown quantities in equation (27) are the angular diameter of the background source θ_s and the distance to the lens D. The angular diameter is $\theta_s \lesssim 1$ mas (Gabuzda et al. 1992, 1994; Gabuzda & Cawthorne 1996; unpublished VLBI data). Toward 0954+658 is Galactic Loop III, which Fiedler et al. (1994b) identify as responsible for the ESE. Its distance is estimated to be 0.15 kpc. More generally, the scale height of the Galaxy's free-electron layer is approximately 1 kpc (Taylor & Cordes 1993). At the Galactic latitude of 0954+658 ($b = 43\overset{\circ}{.}1$), the maximum distance to the lens would be roughly 1.5 kpc.

With these estimates for θ_s and D, we compute a nominal column density through the lens of $N_0 \simeq 0.24$ pc cm^{-3} corresponding to a distance of 0.15 kpc and an upper limit of $N_0 \lesssim 2.4$ pc cm^{-3} corresponding to a distance of 1.5 kpc. Our estimates for θ_s and β_s also provide constraints on the size of the lens. We estimate $\theta_\ell \approx 2.5$ mas, corresponding to $a \approx 0.38$ AU (3.8 AU) for a lens at a distance of 0.15 kpc (1.5 kpc). The free-electron density within the lens is $n_e \approx N_0/a$ or $n_e \sim 10^5$ cm^{-3}; in our model, the electron column density estimate is distance independent. The mass of the lens is $M_\ell \sim m_p n_e a^3$, where m_p is the mass of the proton; for a lens at 0.15 kpc (1.5 kpc), $M_\ell \sim 1.3 \times 10^{20}$ g $\sim 6.5 \times 10^{-14}\, M_\odot$ (1.3×10^{23} g $\sim 6.5 \times 10^{-11}\, M_\odot$).

The angular displacement of the position of the source during the ESE can be estimated from equation (26), $\delta\theta \simeq 250$ mas at 2.25 GHz. Phase-referenced VLBI observations can obtain absolute position information. Angular displacements of this magnitude should be detectable easily, even if the phase-referencing source is a few degrees away (Beasley & Conway 1995). In the case of 0954+658, the radio reference frame source 0951+693 (M81) is roughly 4° away. Of course, if the source is not lensed completely, relative positions between components can be determined with high accuracy, without recourse to phase-referenced observations. We stress that the maximum angular displacement and the optimal time for such observations occur during passage through the outer caustic.

We close this section speculatively. First, we use the linear lens size and the timescale of the ESE to estimate the velocity of the lens. From equation (21), $v \approx 4.3a/\Delta t$. The timescale between the inner caustics of the ESE is $\Delta t \approx 0.25$ yr. Thus, the velocity of the lens is 30 km s^{-1} (300 km s^{-1}) for a lens at 0.15 kpc (1.5 kpc). Second, the lens responsible for the 0954+654 ESE is required to be a factor of a few larger than the source; $\beta_s = 0.4$ implies the angular diameter of the lens is a factor of 2.5 greater than the angular diameter of the lensed source component. However, the lens diameter is also comparable to the size of the jet imaged by Gabuzda et al. (1992, 1994). If the lensed component was indeed a jet component, the lens would have had to pass in front of the jet component without affecting the flat-spectrum core. We therefore suggest that the lens was anisotropic, with the major axis corresponding to the derived lens diameter. The minor axis would have to be smaller than the typical knot separation in the jet, probably less than 1 mas, suggesting an axial ratio of at least 2.5:1. We simply note that anisotropic structures in the interstellar plasma are not unexpected (e.g., Higdon 1984, 1986). Finally, the smooth, single minimum in the 2.25 GHz light curve suggests that the lens encountered only a single com-

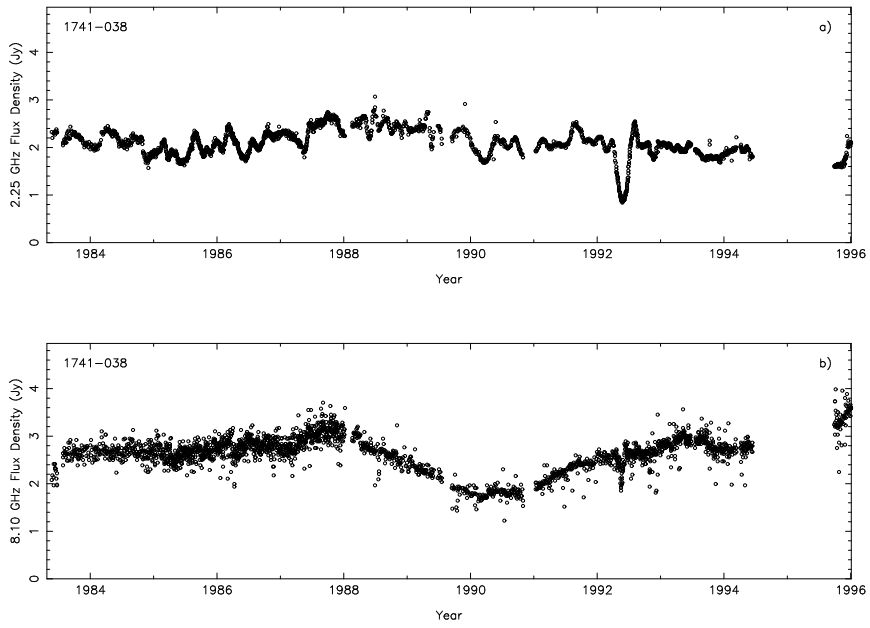

FIG. 10.—Complete light curve of the quasar 1741−038 during the period of observation from 1983 to 1994. The scattering event occurs at approximately 1992 April.

ponent in the jet, i.e., moved northeast-southwest (or vice versa), roughly perpendicularly across the jet axis.

7.2. *1741−038*

The complete light curve for 1741−038 is shown in Figure 10 with the ESE, which occurred in 1992, shown in Figure 11 on an expanded scale. At both frequencies the ESE displays a rounded minimum, with the 2.25 GHz ESE causing an approximately 50% decrease in the source's flux density and the 8.1 GHz ESE causing an approximately 30% decrease in the source's flux density. The lack of a flat bottom and the apparent lack of caustic spikes at either frequency suggest that 1741−038 was only weakly lensed, i.e., no multiple images were formed and $\alpha < \alpha_{\rm min}$.

Our analysis for 1741−038 proceeded in the same fashion as that for 0954+658. Our best model comparison to the 2.25 GHz light curve gives the following parameter values: $\alpha = 2$, $\beta_s = 1.0$, with a single-component (lensed) source model of flux density 2 Jy. The model is superposed on the observational data in Figure 11 and replicates the minimum of the 2.25 GHz event very well. It overestimates the amplitude of the maxima surrounding the minimum, particularly the one preceding the decrease in the source's flux density, but the amplitudes of these maxima are not too much larger than the level of (presumably) intrinsic fluctuations in the light curve.

Scaling the value of α to 8.1 GHz, we find $\alpha = 0.14$. Scaling the source size by λ gives $\beta_s \simeq 0.28$, but Fey et al. (1996) show that the dominant component of 1741−038 is unresolved at this frequency. We therefore assume that $\beta_s = 0$ at 8.1 GHz (in practice, there is very little difference between $\beta_s = 0.28$ and $\beta_s = 0$ light curves). The single component model with $\alpha = 0.14$, $\beta_s = 0$, and lensed source flux density of 2.55 Jy is shown in Figure 11. The observed depth of the light curve is greater than that reproduced by the model, and the observed minimum occurs slightly before that predicted by the model. These deficiencies may indicate that the lens did not pass directly over the source, crossing only at a grazing incidence, that the electron column density within the lens is more complicated than the Gaussian form we have assumed, or that the source contains unresolved substructure.

Following our analysis for 0954+658, we require the

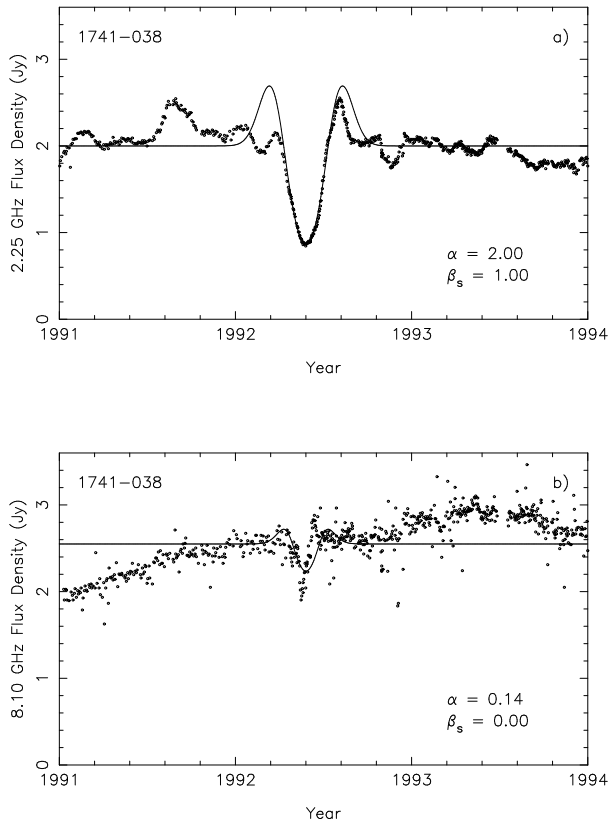

FIG. 11.—Light curves of 1741−038 during an extreme scattering event. (*a*) The dashed line is our model comparison with $\alpha = 2$, $\beta_s = 1$, and a flux density for 1741−038 of 2 Jy at 2.25 GHz. (*b*) The model uses $\alpha = 0.14$, $\beta_s = 0$, and assumes an 8.1 GHz flux density of 2.55 Jy.

source size and distance to the lens in order to constrain N_0, equation (27). Fey et al. (1996) show that the angular size of 1741−038 is approximately 0.5 mas at 2.32 GHz. Since $\beta_s = 1$, the lens must also be approximately 0.5 mas in diameter. A number of sources displaying ESEs, including 1741−038, are seen along the edges of radio Loop I (Fiedler et al. 1994a). Berkhuisjen (1973) estimates a distance of 130 ± 75 pc to Loop I. If we assume that the ESE arises from a structure associated with Loop I, the resulting peak electron column density through the lens is $N_0 \simeq 10^{-4}$ pc cm^{-3}. If we do not associate the ESE with Loop I, we can place a limit on its distance only by requiring that the lens be within one scale height of the free-electron layer of the Galaxy. This distance limit is $D \lesssim 4.5$ kpc, for a peak column density of $N_0 \lesssim 3.6 \times 10^{-3}$ pc cm^{-3}. Although a connection between Loop I and the ESEs is suggestive, the line of sight to 1741−038 (and other, nearby sources which have undergone an ESE) passes through the inner Galaxy, and some other Galactic structure may be responsible for the ESEs.

The inferred size of the lens is 0.065 AU ($\lesssim$2.25 AU), if the lens is (is not) associated with Loop I. The density within the lens is $n_e \approx 300$ cm^{-3}, for a corresponding mass of 1.6×10^{15} g $\sim 8 \times 10^{-19}$ $M_\odot$ (6.8×10^{19} g $\sim 3.4 \times 10^{-14}$ $M_\odot$) if the lens is (is not) associated with Loop I. The timescale between the maxima is 0.4 yr. The corresponding velocity of the lens is 3 km s^{-1} ($\lesssim$110 km s^{-1}) for a lens associated (not associated) with Loop I.

These lens parameters are comparable to those derived for the ESE for PSR B1937+21 (Cognard et al. 1993): $N_0 = 6.5 \times 10^{-5}$ pc cm^{-3} and $a \approx 0.07$ AU. (They actually fit for two lenses; we quote the total electron column density through both lenses and the mean size of the two lenses.)

As we indicated in § 6, angular displacement occurs regardless of the value of α. Thus, even though caustic surfaces were not formed during lensing of 1741−038, we can still apply equation (26). We find the maximum angular displacement during the ESE to be approximately 0.4 mas at 2.25 GHz and 0.03 mas at 8.1 GHz. It is unlikely that these angular displacements could be measured using phase-referenced observations. Relative position shifts of this magnitude between lensed and unlensed components might be detectable at 2.25 GHz, particularly if the source structure could be determined soon after the ESE so that proper motion of the components is negligible.

Clegg et al. (1996) conducted polarization observations of 1741−038 with the VLA during and after the ESE in an effort to detect changes in Faraday rotation as a result of the lens passing across the line of sight. No rotation measure change was detected to a level of $\Delta\mathrm{RM} \lesssim 10$ rad m^{-2}. The rotation measure change is given by

$$\Delta\mathrm{RM} \simeq 0.81 \langle B_\parallel \rangle N_0 \,, \tag{28}$$

where $\langle B_\parallel \rangle$ is the mean component of the magnetic field within the lens parallel to the line of sight in microgauss. Our derived value of N_0 is consistent with the lack of observed change in RM, since the mean parallel magnetic field component would have to be $\langle B_\parallel \rangle \gtrsim 120$ mG (3.5 mG), if the lens is (is not) associated with Loop I, in order for a change in RM to have been detected. These magnetic field levels are 10^3–10^5 times larger than those typical of the interstellar medium. If the lens is *not* associated with Loop I, Clegg et al. (1988) have shown that magnetic field levels $B \gtrsim 2$ mG can be encountered as the result of strong interstellar shocks; however, if the lens is associated with Loop I, the magnetic field required to produce an observable change in RM is still a factor of 60 larger than what can plausibly be produced.

8. CONCLUSIONS

We have presented the geometric optics for refraction by an interstellar plasma lens, with specific application to a lens with Gaussian profile of free-electron column density. We have shown that the one-dimensional refractive properties of a lens can be characterized completely by two dimensionless parameters. The first parameter characterizes the refractive power of the lens and is

$$\alpha = 3.6 \left(\frac{\lambda}{1 \text{ cm}} \right)^2 \left(\frac{N_0}{1 \text{ cm}^{-3} \text{ pc}} \right) \left(\frac{D}{1 \text{ kpc}} \right) \left(\frac{a}{1 \text{ AU}} \right)^{-2} , \tag{15}$$

where λ, N_0, D, and a are the wavelength of observation, maximum free-electron column density, distance from lens to observer, and size of the lens transverse to the line of sight, respectively. The second parameter characterizes the extent to which the effect of the lens is diminished by the intrinsic size of the source and is

$$\beta_s = \theta_s / \theta_\ell \,, \tag{13d}$$

which is the relative angular size of the background source θ_s compared to the angular size of the lens θ_ℓ as seen by the observer.

The effect of the plasma lens is to enhance or reduce the observed brightness of the background source due to focusing or spreading of ray bundles, and to change the apparent position of the background source due to refraction. The minimum brightness of the background source occurs directly on the lens axis. For a point source, $\beta_s = 0$, the on-axis brightness will be $1/(1 + \alpha)$ of its nominal (unlensed) brightness.

On either side of the lens axis, at a distance determined by the value of α, the background source will have a maximum intensity due to focusing of ray bundles. If $\alpha \geq \alpha_{\min} \simeq 2.25$, the focusing of ray bundles will become strong enough for ray paths to cross, and multiple imaging of the background source will occur. For the case of a Gaussian lens profile, an observer located within a region of multiple imaging can see as many as three images of the background source, each with a different brightness and appearing to come from slightly different directions. The total brightness of the source, obtained by adding the brightness of the multiple images, will be greater than the nominal brightness of the source.

Separating the multiple-imaging regions from the single-image regions are caustic surfaces, on which two of the three multiple images blend together and, in the limit of geometrical optics, the observed brightness of the background source grows without bound. An observer passing from a single-image region through the multiple-imaging regions and back to a single-image region can use the observed position of the caustics to determine the magnitude of the parameter α. The separation between the *inner* caustics can also be used to constrain the diameter of the lens.

The primary effect of increasing the angular size of the background source in relation to the angular size of the lens, i.e., increasing β_s, is to smooth out the light curve and reduce the observed amplitudes of maximum and minimum intensity.

We have generated sample light curves from our model and compared them to extreme scattering events observed toward the extragalactic sources 0954+658 (§ 7.1) and 1741−038 (§ 7.2). These two sources were chosen because their ESEs have the highest quality data available and, in the case of 1741−038, polarization observations also exist. In general we find reasonable agreement between the observed and modeled light curves at 2.25 GHz. We have far more difficulty re-creating the 8.1 GHz light curves by utilizing only the appropriate wavelength scalings for α and β_s. The discrepancies between the modeled and observed light curves may result from some combination of substructure within the lens, an anisotropic lens shape, a lens that only grazes the source rather than passing completely over it, or unresolved substructure within the extragalactic sources.

For 0954+658 we find it to be strongly lensed at 2.25 GHz. Interpreting the light curve for this source is difficult because of uncertainties about the source's structure at the time of the ESE. We favor an interpretation in which the lens passed over a component in the source's jet. The lens toward this source is probably associated with radio Loop III so that the lens was 0.15 kpc distant. The peak column density in the lens was 0.24 pc cm^{-3}, its size was 0.38 AU the electron density within the lens is 10^5 cm^{-3}, and its mass was 6.5×10^{-14} $M_\odot$. The lens also caused the source's position to wander by as much as 250 mas at 2.25 GHz, an easily detectable amount using phase-referenced VLBI observations or by measuring the relative positions between source components.

For 1741−038, the ESE was caused by a weak lens. The lens toward this source is likely to be associated with radio Loop I and at a distance of 0.13 kpc. The peak column density of the lens is 10^{-4} pc cm^{-3}, its size is 0.065 AU, density 300 cm^{-3}, and mass 10^{-18} $M_\odot$. From Clegg et al.'s (1996) upper limit on the change in Faraday rotation toward 1741−038 during the ESE, we place an upper limit of approximately 100 mG on the magnetic field within the lens. The angular position wander caused by this lens was only 0.4 mas at 2.25 GHz. An angular displacement of this magnitude would not have been detectable for 1741−038; many other sources that have undergone ESEs have more complicated structures than 1741−038, however, and relative position shifts of this magnitude between lensed and unlensed components might be detectable in those sources. These lens parameters are comparable, within 50%, to those derived for the ESE for PSR B1937+21 (Cognard et al. 1993): $N_0 = 6.5 \times 10^{-5}$ pc cm^{-3} and $a \approx 0.07$ AU. (They actually fit for two lenses; we quote the total electron column density through both lenses and the mean size of the two lenses.)

A key assumption of our plasma lens explanation for ESEs is that the lenses are discrete objects. The lens properties we have derived are consistent with this assumption. If we assume the plasma temperature within the lenses to be 10^4 K, the pressure within the lenses is $nT \sim 3 \times 10^6$–10^9 K cm^{-3}. These pressures are well in excess of the average ISM pressure of roughly 4000 K cm^{-3} (Kulkarni & Heiles 1988). Such lenses either would be highly transitory features or would be embedded in high-pressure environments. Romani et al. (1987) suggest ionization fronts, cooling instabilities, or both associated with old supernova remnants as sites of lenses.

We emphasize that the difficulties in interpreting the light curve for future ESEs could be ameliorated considerably by VLBI imaging of a source as soon as possible after, or indeed during, an ESE. Considerable angular displacements might also be detected with such observations.

We thank J. Cordes for guidance at the beginning of this project and the referee, D. Gabuzda, for comments which helped us clarify a number of the points in this paper. A portion of this work was performed while T. J. W. L. held a National Research Council–Naval Research Laboratory Research Associateship. Basic research in astronomy at the Naval Research Laboratory is supported by the Office of Naval Research.

REFERENCES

Beasley, A. J., & Conway, J. E. 1995, in Very Long Baseline Interferometry and the VLBA, ed. J. A. Zensus, P. J. Diamond, & P. J. Napier (San Francisco: ASP), 327
Berkhuisjen, E. M. 1973, A&A, 24, 143
Born, M., & Wolf, E. 1980, Principles of Optics (6th ed.; Oxford: Pergamon)
Clegg, A. W., Chernoff, D. F., & Cordes, J. M. 1988, in Radio Wave Scattering in the Interstellar Medium, ed. J. M. Cordes, B. J. Rickett, & D. C. Backer (New York: AIP), 174
Clegg, A. W., Fey, A. L., & Fiedler, R. L. 1996, ApJ, 457, L23
Clegg, A. W., Fiedler, R. L., & Cordes, J. M. 1993, ApJ, 409, 691
Cognard, I., Bourgois, G., Lestrade, J.-F., Biraud, F., Aubry, D., Darchy, B., & Drouhin, J.-P. 1993, Nature, 366, 320
Fey, A. L., Clegg, A. W., & Fiedler, R. L. 1996, ApJ, 468, 543
Fiedler, R. L., Dennison, B., Johnston, K. J., & Hewish, A. 1987, Nature, 326, 675
Fiedler, R., Dennison, B., Johnston, K. J., Waltman, E. B., & Simon, R. S. 1994a, ApJ, 430, 581
Fiedler, R., Pauls, T., Johnston, K. J., & Dennison, B. 1994b, ApJ, 430, 595
Gabuzda, D. C., & Cawthorne, T. V. 1996, MNRAS, 283, 759
Gabuzda, D. C., Cawthorne, T. V., Roberts, D. H., & Wardle, J. F. C. 1992, ApJ, 388, 40
Gabuzda, D. C., Mullan, C. M., Cawthorne, T. V., Wardle, J. F. C., & Roberts, D. H. 1994, ApJ, 435, 140
Gupta, Y., Rickett, B. J., & Lyne, A. 1988, in Radio Wave Scattering in the Interstellar Medium, ed. J. M. Cordes, B. J. Rickett, & D. C. Backer (New York: AIP), 140
Hewish, A., Wolszczan, A., & Graham, D. A. 1985, MNRAS, 213, 167
Higdon, J. C. 1984, ApJ, 285, 109
———. 1986, ApJ, 309, 342
Kollgaard, R. I., Wardle, J. F. C., Roberts, D. H., & Gabuzda, D. C. 1992, AJ, 104, 1687
Kulkarni, S. R., & Heiles, C. 1988, in Galactic and Extragalactic Radio Astronomy, ed. G. L. Vershuur & K. I. Kellermann (Berlin: Springer), 95
Pearson, T. J., & Readhead, A. C. S. 1988, ApJ, 328, 114
Rickett, B. J. 1990, ARA&A, 28, 561
Romani, R. W., Blandford, R. D., & Cordes, J. M. 1987, Nature, 328, 324
Taylor, J. H., & Cordes, J. M. 1993, ApJ, 411, 674
Wolszczan, A., & Cordes, J. M. 1987, ApJ, 320, L35